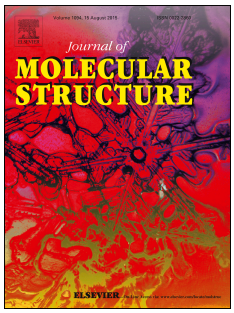

Synthesis, crystal structure, hirshfeld surface analysis, DFT computations and molecular dynamics study of 2-(benzyloxy)-3-phenylquinoxaline

Nadeem Abad, Hassane Lgaz, Zeliha Atioglu, Mehmet Akkurt, Joel T. Mague, Ismat H. Ali, Ill-Min Chung, Rachid Salghi, El Mokhtar Essassi, Youssef Ramli

PII: S0022-2860(20)31052-8

DOI: https://doi.org/10.1016/j.molstruc.2020.128727

Reference: MOLSTR 128727

To appear in: *Journal of Molecular Structure*

Received Date: 16 December 2019

Revised Date: 9 June 2020

Accepted Date: 17 June 2020

Please cite this article as: N. Abad, H. Lgaz, Z. Atioglu, M. Akkurt, J.T. Mague, I.H. Ali, I.-M. Chung, R. Salghi, E.M. Essassi, Y. Ramli, Synthesis, crystal structure, hirshfeld surface analysis, DFT computations and molecular dynamics study of 2-(benzyloxy)-3-phenylquinoxaline, *Journal of Molecular Structure* (2020), doi: https://doi.org/10.1016/j.molstruc.2020.128727.

Author contributions section

Nadeem Abad, Hassane Lgaz, Zeliha Atioglu, Mehmet Akkurt: Performed experiments and calculations, analyzed the data, and wrote the initial manuscript.

Joel T Mague, Rachid Salghi, Ismat H. Ali and Youssef Ramli: Contributed data or analysis tools, formal analysis, resources, Project administration, review&editing.

El Mokhtar Essassi, Ill-Min Chung and Youssef Ramli: Conceptualization, methodology, supervision, review&editing.

Graphical abstract:

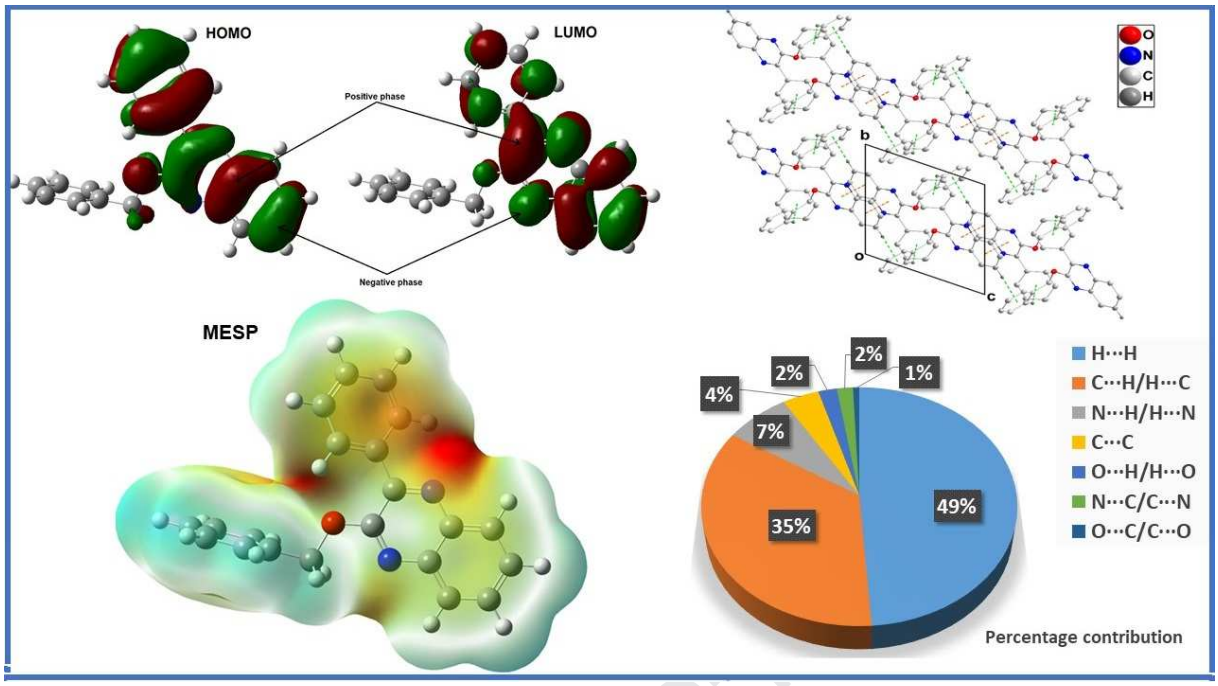

Synthesis, Crystal Structure, Hirshfeld Surface Analysis, DFT computations and Molecular Dynamics Study of 2-(benzyloxy)-3-phenylquinoxaline

Nadeem Abad[1,2,a], Hassane Lgaz[3,a], Zeliha Atioglu[4], Mehmet Akkurt[5], Joel T. Mague[6], Ismat H. Ali[7], Ill-Min Chung[3], Rachid Salghi[8,*], El Mokhtar Essassi[2] and Youssef Ramli[1*]

"[1]Laboratory of Medicinal Chemistry, Drug Sciences Research Center, Faculty of, Medicine and Pharmacy, Mohammed V University, Rabat, Morocco.
[2]Laboratoire de Chimie Organique Heterocyclique URAC 21, Faculté des Sciences, Mohammed V University, Rabat, Morocco.
[3]Department of Crop Science, College of Sanghur Life Science, Konkuk University, Seoul 05029, South Korea.
[4]Ilke Education and Health Foundation, Cappadocia University, Cappadocia, Vocational College, the Medical Imaging Techniques Program, 50420 Mustafapasa, Ürgüp, Nevsehir, Turkey.
[5]Department of Physics, Faculty of Sciences, Erciyes University, 38039 Kayseri, Turkey.
[6]Department of Chemistry, Tulane University, New Orleans, LA 70118, USA.
[7]Chemistry Department, College of Science, King Khalid University, Abha 61413, Saudi Arabia.
[8]Laboratory of Applied Chemistry and Environment, ENSA, University Ibn Zohr, PO Box 1136, Agadir, Morocco"

*Corresponding authors:

Youssef Ramli, Email: y.ramli@um5s.net.ma**, Rachid Salghi**, Email: r.salghi@uiz.ac.ma,

[a]Have equal contribution in this work

Abstract

Quinoxalines are regarded as a promising class of biologically active agents, and they constitute useful intermediates in organic synthesis. In this study, we report synthesis, single crystal X-ray diffraction, and computational investigations of the 2-(benzyloxy)-3-phenylquinoxaline (*O*-alkylated isomer). Single crystal X-ray diffraction investigations

revealed that the quinoxaline unit is not entirely planar. In the crystal form, inversion-related molecules form dimers through slipped π-stacking interactions between quinoxaline units. These are coupled together into chains extending along the c-axis direction by C—H···π(ring) interactions. Inspection of the Hirshfeld surface analysis revealed that H···H (48.8%), C···H/H···C (35.1%) and H···N/N···H (7.3%) are the main interactions that govern the crystal packing of the presented structure. The optimized geometry, Natural Bond Orbital (NBO), Fukui functions and all other structural and electronic features were calculated by using Density Functional Theory (DFT) at B3LYP employing 6-311++G(d,p) basis set. The HOMO and LUMO distribution showed a pronounced electronic density over the quinoxaline moiety. Computed NBO analysis explored the interactions as well as charge transfers among different orbitals and lone pairs occurring within the compound. Radial distribution functions (RDF) were calculated using molecular dynamics (MD) simulations to study interactions of water molecules with atoms of the title compound.

Keywords: Crystal structure; quinoxaline; DFT; Fukui function; Hirshfeld surface; Radial distribution functions.

1. Introduction

Quinoxaline derivatives are a class of organic compounds comprising a large group of nitrogen-containing heterocycles. They are of significant importance and high practical value for the development of potent pharmacologically active compounds [1–3]. These compounds are known to possess a wide spectrum of biological activities, including antibacterial [4], HIV [5], antimicrobial [6], anti-inflammatory [7], antiprotozoal [8], and anticancer [9]. There now exists a plethora of reports describing different biological and photo-physical properties possessed by quinoxaline-based compounds [10–13].

Echinomycin is a natural antibiotic belonging to the quinoxaline antibiotic family, which exhibit various potent antimicrobial properties [14]. Subsequently, further synthetic modifications of echinomycin were undertaken to develop several novel quinoxaline antibiotics [11]. Furthermore, many drug candidates bearing diversely substituted quinoxalines have been used for the development of new anticancer therapeutic agents and some of them are under clinical trials [11]. Besides, quinoxaline and its derivatives have numerous applications in many fields, such as agrochemicals as pesticides [15], insecticides [16], herbicides [17], electron-transporting materials [18,19], building blocks in electroluminescent and photoluminescent materials [20].

The numerous applications of quinoxalines have prompted researchers to explore and develop efficient methods to synthesize new derivatives likely to present exciting activities [21]. Alkylation reactions were used to synthesize bioactive compounds for the development of new drug molecules, particularly the alkylation under the conditions of phase transfer catalysis (PTC).

In view of the above-mentioned considerations, and as a continuation of our research work [22–24], we are reporting here the synthesis of 2-(benzyloxy)-3-phenylquinoxaline, using the alkylation reaction under the conditions of solid-solid PTC, which allowed us to isolate the *O*-alkylated product (Figure 1a). The crystal structure of 2-(benzyloxy)-3-phenylquinoxaline was then obtained and reported. Its structure was characterized computationally with the DFT method at B3LYP employing 6-311++G(d,p) basis set and the Hirshfeld surface analysis. The HOMO and LUMO, which are known as Frontier Molecular Orbitals (FMOs) along with other chemical descriptors, were examined to evaluate the reactivity of the synthesized compound. Local reactivity (Fukui functions and dual descriptor), MEP, and net charges were also calculated and discussed. The NBO analysis

was carried out to calculate the net electron transfer from donors to acceptors, while the RDF was used to determine atoms with significant interactions with water molecules.

2. Materials and methods

2.1. General Information

All the reagents used for the synthesis were commercially available (Sigma-Aldrich, Merck) and employed without further purification. For analytical TLC, silica gel aluminum plates (Merck 60 F_{254}) were used. NMR spectra (^{1}H NMR and ^{13}C NMR) were processed with Bruker Avance 300 NMR Spectrometer operating at 300 and 75 MHz, respectively, in deuterated chloroform ($CDCl_3$) as solvent and TMS as an internal standard.

2.2. Synthesis of 2-(benzyloxy)-3-phenylquinoxaline

3-Phenylquinoxalin-2(1H)-one (1 g, 4.5 mmol), benzyl chloride (0.77ml, 6.75 mmol), and potassium carbonate (0.931g, 6.75 mmol) with the amount of catalytic tetra-n-butylammonium bromide (0.29g, 0.9mmol) were stirred in N, N-dimethylformamide (DMF) (20 ml) for 48 h (Scheme 1). The solution was filtered, and the solvent was allowed to evaporate under vacuum. Dichloromethane (20 ml) was added, and the solution was filtered. The residue product was chromatographed on a silica gel column (hexane / ethyl acetate: 9/1, as mobile phase) to give two different fractions.

The first fraction was purified by recrystallization in ethanol to afford yellow crystals with a yield of 33% (O-alkylated isomer) while recrystallization of the second fraction gave a yellowish powder with a yield of 48.5% (*N*-alkylated isomer). IR spectra of *O*- and *N*-

alkylated isomers are shown in Figures S1 and S2 (Supplementary material), while the UV-Vis spectra of the *O*-alkylated isomer is shown in Figure S3.

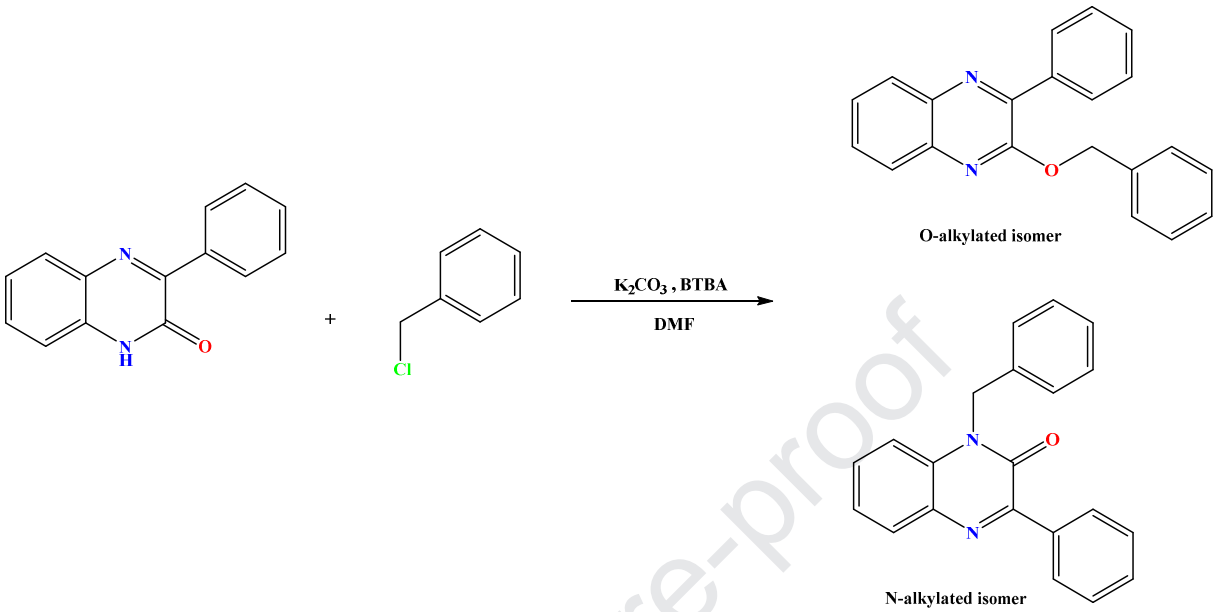

Scheme 1. Synthesis procedure of 2-(benzyloxy)-3-phenylquinoxaline and its isomer.

***O*-alkylated isomer : Mp =** 97-99 **°C** , **FT-IR (KBr):** 3083 cm^{-1} (aromatic CH), 2931 (aliphatic CH), 1585 (C=N), **^{1} H NMR** (300 MHz, $CDCl_3$-d6) δ ppm: 5.70(s, 2H, O-CH_2); 7.37-7.54 (m, 5$H_{aromatic}$); 7.52-8.20 (m, 9$H_{aromatic}$); **^{13}C NMR** (75 MHz, 110 $CDCl_3$) δ ppm:67.73 (CH_2); 126.72, 126.88, 127.96, 128.01, 128.22, 128.52, 129.06, 129.68, 129.73, 129.76 ($CH_{aromatic}$); 136.04, 136.63, 139.10, 139.84, 146.60 (Cq); 155.24 (C-O). **^{1} H NMR** and **^{13}C NMR** spectrums of the *O*-alkylated isomer are shown in Figures S4-S6.

***N*-alkylated isomer : Mp =** 121-123 **°C, FT-IR (KBr):** 3111 cm^{-1} (aromatic CH), 2950 (aliphatic CH), 1625 cm^{-1} (C=O), 1585 (C=N), **^{1} H NMR** (300 MHz, $CDCL_3$) δ ppm:5.50(s, 2H, N-CH_2); 7.17-7.37 (m, 5$H_{aromatic}$); 7.41-8.30 (m, 9$H_{aromatic}$); **^{13}C NMR** (75 MHz, $CDCL_3$-d6) δ ppm:46.15 (CH_2); 114.38, 123.82, 127.01, 127.72, 128.13, 128.96, 129.68, 130.33, 130.45, 130.62($CH_{aromatic}$); 132.78, 133.36, 135.40, 136.05, 154.24(Cq); 155.82 (C=O).

2.3. Data collection and refinement details

Data collection of *O*-alkylated isomer was performed using a Bruker Smart APEX CCD system using Mo-K_α radiation (λ = 0.71073 Å). In this compound, all H atoms were located in a difference-Fourier map and were freely refined. The structure solution was solved employing SHELXT [25] and refinements were carried out on F^2 by full-matrix least-squares techniques using SHELXL [25]. The experimental details, including structure refinement and data collection details for *O*-alkylated isomer, are summarized in Table S1 (Supplementary Material).

2.4. Computational details

Optimization of molecular geometry was performed using the Gaussian 09W package [26]. GaussView molecular visualization software was used to draw the initial structure and to visualize the results [27]. The molecular structure of the 2-(benzyloxy)-3-phenylquinoxaline was optimized using the DFT method at B3LYP employing 6-311++G (d,p) basis set, default SCF and geometrical convergence criteria in the water phase [28–30]. The solvent effect in aqueous phase has been performed using the self-consistent recognition reaction field (SCRF) method as implemented in the integral equation formalism polarized continuum model (IEFPCM). For comparison purpose, quantum chemical parameters of *N*-alkylated isomer were also computed and represented. Information about the delocalization of charge in the synthesized compound was provided through NBO analysis using NBO Ver. 3.1 (Implemented in Gaussian Software) at the same DFT level with the POP=NBO keyword. Chemical reactivity of the compound was discussed in view of the global reactivity descriptors, HOMO-LUMO energies, MEP, natural and Mulliken charges. In order to

validate the experimental results, IR spectra was also determined. Both experimental and theoretical spectra are represented in supplementary material (Figure S1), from which a good agreement can be seen between predicted and experimental data. Electronic transitions in the UV-Vis spectral region were calculated by time dependent (TD) DFT method with CAM-B3LYP level and 6-311++G (d, p) basis set in the ethanol. The comparison between simulated and experimental ultraviolet–visible spectra is shown in Figure S3, which shown a good agreement. It should be noted that DFT and experimental UV-vis spectra were determined for single crystals.

Local reactivity descriptors were investigated by performing Fukui functions and dual descriptor calculation using the GGA functional according to Perdew, Burke, and Ernzerhof (PBE) and the DNP basis set [31] packed in Dmol3 module of Materials Studio (MS) software [32]. Radial distribution function (RDF) was determined using molecular dynamics simulations, aiming to investigate interactions of water molecules with atoms of the synthesized quinoxaline derivative. To this end, a cubic simulation box containing one title molecule and ~3000 water molecules was constructed and simulated at a temperature of 300 K, and pressure of 1.01325 bar with a timing increment of 1 fs, simulation duration of 10 ns and a 12 Å cut off a radius. Simulations were performed by applying the COMPASS force field within the isothermal–isobaric (NPT) ensemble [33]. It should be noted that the simulation box was relaxed in the beginning for a 100 ps within the canonical (NVT) ensemble.

3. Results and discussions

3.1. Description of the crystal structure and optimized geometry results

3-Phenylquinoxalin-2(1H)-one is in tautomeric equilibrium with its isomer 3-phenylquinoxalin-2-ol, which led to the formation of two isomers during the akylation reaction with benzyl chloride. These are the *N*-alkylated isomer in powder form with a yield of 48.5% and the *O*-alkylated isomer in the form of crystals with a yield of about 33%. Crystals of the title compound were grown by ethanol evaporation, and a crystal structure was obtained (Figure 1(a)). The quinoxaline unit (N13/N14/C1–C6/C11-C12) is not quite planar [r.m.s deviation = 0.001 Å]. The phenyl substituent (C15–C18, C20, C22) is aligned at 39.32 (5)° with respect to the mean plane through the quinoxaline unit, whereas the phenyl ring (C29–C32, C34, C36) of the benzyloxy moiety is aligned at 79.98 (5)°. The C12—O40—C26—C29 torsion angle is 97.06 (11)°.

In this structure, the molecule is stabilized by two weak intramolecular C—H···O contacts, forming C(5) and C(6) ring motifs (Table 1) [34]. In the crystal, inversion-related molecules form dimers through slipped π-stacking interactions between quinoxaline units with a centroid···centroid distance of 3.5979 (9) Å and the dihedral angle between mean planes of 1.25 (6)° (Figures 2, S7 and S8). The dimers are connected into chains extending along the c-axis direction by C1—H7···Cg3 and C30—H33···Cg4 interactions (Table 1 and Figures 2, S7 and S8). The chains pack with normal van der Waals contacts (Figures 2 & S7).

Cg1 and Cg2 are, respectively, the centroids of the N13/C3/C4/N14/C11/C12 and the C1...C6 rings. The centroid...centroid distance Cg1...Cg2 (at 1-x,1-y,2-z) is the same as for the Cg2...Cg1 (at 1-x,1-y,2-z) and is the value given in the CIF. The C2...Cg1 (at 1-x,1-y,2-z) distance is 3.44 Å while the N13...Cg2 (at 1-x,1-y,2-z) distance is 3.41 Å.

199 **Table 1.** Hydrogen-bond geometry (Å, °)

D—H···*A*	*D*—H	H···*A*	*D*···*A*	*D*—H···*A*
C31—H35···O40	0.988 (16)	2.467 (15)	2.8346 (15)	101.5 (11)
C16—H19···O40	1.031 (16)	2.383 (16)	2.8529 (17)	106.5 (10)
C1—H7···Cg3^{i}	0.959 (16)	2.670 (18)	3.5285 (15)	149.2 (15)
C30—H33···Cg4^{ii}	0.999 (16)	2.948 (18)	3.7966 (16)	140.1 (12)

Cg3 and Cg4 are, respectively, the centroids of the C29···C31 and the C15···C17 phenyl rings; Symmetry codes: (i) x, y, z+1; (ii) −x+1.

202

203 Theoretically predicted geometrical parameters, i.e. (bond lengths, bond angles, and torsion
204 angles), are listed in Table 2 along with those from X-ray structure analysis. The optimized
205 molecular structure of 2-(benzyloxy)-3-phenylquinoxaline showing the atom numbering
206 scheme, is represented in Figure 1(b).
207 Unlike the X-ray structure analysis, the theoretically predicted parameters were calculated
208 in a simulated water phase, which is so far from the experimental environment. It is worth
209 considering this when comparing both results, and therefore small deviations should not be
210 surprising. However, the results demonstrate a good agreement between both data, which
211 is confirmed by correlation coefficients of 0.991 and 0.976 for bond lengths and bond
212 angles, respectively.

213

214 **Table 2**. Some selected experimental and theoretical geometric parameters for 2-
215 (benzyloxy)-3-phenylquinoxaline (Å, °).

Geometric Parameters	**Experimental [X–ray diffraction]**	**Theoretical [DFT/B3LYB]**
Bond (Å)		
O40-C12	1.3464(12)	1.34944
N13-C12	1.3031(13)	1.30571
N14-C11	1.3131(13)	1.31705
C4-C5	1.4106(15)	1.41697
C5-C6	1.3735(15)	1.37113
C6-C1	1.4080(17)	1.41653
C1-C2	1.3740(16)	1.38235
C2-C3	1.4124(15)	1.41449

C12-C11	1.4551(15)	1.45837
C26-C29	1.5089(15)	1.50505
O40-C26	1.4475(13)	1.44263
N13-C3	1.3755(14)	1.36769
N14-C4	1.3749(13)	1.36466
C4-C3	1.4139(16)	1.41401
C11-C15	1.4888(14)	1.48839
R^2=0.991		
Bond angles (º)		
C12-O40-C26	118.14(8)	117.38198
C11-N14-C4	118.06(9)	118.72634
N14-C4-C3	121.23(10)	120.60224
C6-C5-C4	120.01(10)	120.94389
C2-C1-C6	120.42(10)	120.73123
N13-C3-C2	119.83(10)	120.38275
C2-C3-C4	119.55(10)	119.58553
N13-C12-C11	123.49(10)	123.18501
N14-C11-C12	119.80(10)	118.54829
C12-C11-C15	122.74(9)	122.21587
C12-N13-C3	116.79(9)	116.89647
N14-C4-C5	119.36(10)	119.83692
N13-C3-C4	120.62(10)	120.03068
N13-C12-O40	120.89(9)	119.64714
O40-C12-C11	115.59(9)	115.15772
N14-C11-C15	117.45(9)	117.21057
O40-C26-C29	112.66(9)	111.76381
R^2=0.976		
Torsion angles (º)		
C11-N14-C4-C5	-178.21(10)	-179.51737
N14-C4-C5-C6	179.21(10)	179.61686
N13-C12-C11-C15	179.52(9)	178.99326
C26-O40-C12-C11	177.94(9)	176.90779
N14-C4-C3-N13	-0.69(16)	0.72309

3.2. Hirshfeld surface analysis

Hirshfeld surfaces (HS) were generated for the title compound using CrystalExplorer17.5 [35]. Hirshfeld surfaces enable the visualization of inter-molecular interactions by different colors and color intensity, representing short or long contacts and indicating the relative strength of the interactions.

The function d_{norm} is a ratio enclosing the distances of any surface point to the nearest interior (d_i) and exterior (d_e) atom and the van der Waals radii of the atoms [36,37]. The function d_{norm} will be equal to zero when intermolecular distances are close to van der Waals contacts. They are indicated by a white color on the Hirshfeld surface, while contacts longer than the sum of van der Waals radii with positive d_{norm} values are colored in blue. The surface plot for d_{norm} (Figure S9) was generated using a high standard surface resolution over a color scale of -0.1330 to 1.3108 a.u.

The bright-red spots indicate their roles as the respective donors and/or acceptors; they also appear as blue and red regions corresponding to positive and negative potentials on the Hirshfeld surface mapped over electrostatic potential shown in Figure S10. The blue regions indicate the positive electrostatic potential (hydrogen-bond donors), while the red regions indicate the negative electrostatic potential (hydrogen-bond acceptors) [38,39]. The shape index of the Hirshfeld surface is a tool to visualize π–π stacking interactions by the presence of adjacent red and blue triangles. If there are no adjacent red and/or blue triangles, then there are no π–π interactions. Figure S11 clearly suggests that there are π–π interactions present in the title compound.

Figure 3a shows the overall 2D fingerprint plot, and Figure 3b-d shows those for the H···H, C···H / H···C, and N···H / H···N interactions, respectively [40]. The H···H contribution is 48.8% to the overall molecular packing (Figure 3b). The wide peak at $d_i = d_e = 1.15$ Å in Figure 3b is due to the short interatomic H···H interactions (Table 3). The existence of two C—H···π interactions (Table 1) eventuate as two pairs of wings in the fingerprint plot delimited into C···H/H···C interactions with a 35.1% contribution to the HS analysis (Figure 3c). However, the two pairs of thin and thick edges at $d_i + d_e = 2.60$ Å, arise from the interatomic C···H/H···C interactions (Table 3).

Figure 4a-d represents the contributions to the HS for all···all, H···H, C···H/H···C, and N···H/H···N interactions, respectively. In the crystal structure, the H···N/N···H interactions with 17.0 % contribution have a symmetrical point distribution as shown in Figure 4d, with the ends at $d_e + d_i$ = 2.80 Å (Table 4). The interatomic C···C interactions (Table 4) with a 4.1% contribution shown as an arrow-shaped point distribution in Figure 4c, with the vertex at $d_i = d_e$= 1.65 Å. The percentage contributions of the remaining interatomic interactions to the HS for the title compound are listed in Table 4 and are presented in Figure 5.

The HS analysis verifies the significance of H-atom interactions in setting up the molecular packing. The H···H, C···H/H···C, and N···H/H···N interactions state that hydrogen bonding and van der Waals interactions play the leading roles in the molecular packing [40].

Table 3. Summary of short interatomic contacts (Å) in the title compound.

Contact	Distance	Symmetry operation
(C26) H27···O40 (C12)	2.66	1 - x, 1 - y, 1 - z
(C18) H23···C4 (N14)	2.84	- x, 1 - y, 1 - z
(N13) C3···C3 (N13)	3.42	1 - x, 1 - y, 2 - z
(C5) H9···C5 (C4)	3.08	- x, 1 - y, 2 - z
(C6) H10···H16 (C19)	2.44	x, y, 1 + z
(C2) H8···H24 (C20)	2.48	x, - 1 + y, z
(C34) H38···C36 (C34)	3.05	- x, - y, - z
(C36) H39···H9 (C5)	2.39	x, - 1 + y, - 1 + z
(C32) H37···H28 (C26)	2.53	1 - x, - y, 1 - z

Table 4. Percentage contributions of interatomic contacts to the Hirshfeld surface for the title compound.

Contact	Percentage contribution
H···H	48.8
C···H/H···C	35.1
N···H/H···N	7.3
C···C	4.1
O···H/H···O	2.1
N···C/C···N	1.8

O···C/C···O	0.7

3.4. Frontier molecular orbital (FMO) studies

The chemical reactivity of an organic compound at the atomic level can be assessed through examination of the molecular orbitals [41–44]. Bultinck et al. [45] stated that "*The energies of the highest occupied molecular orbital and the lowest unoccupied molecular orbital (HOMO and LUMO energies) belong to the most popular quantum chemical descriptors*". As it is well known, HOMO is the outermost orbital that provides information on the tendency of a molecule to donate electrons; meanwhile, the innermost orbital LUMO is related to the electron affinity, and it is an indicator of the electron-accepting ability of a chemical compound [43,46,47]. The 3D plot of HOMO and LUMO orbitals of the title compound is shown in Figure 6. As can be observed from Figure 6, the LUMO and HOMO electrons have similar distributions, which are all delocalized on the quinoxaline moiety and the phenyl ring linked to it. It means that they are the preferred regions for donating and accepting electrons.

Based on the frontier molecular orbitals (FMOs), the ionization energy (IP) and electron affinity (EA) can be determined by the following formulas [48]:

$$EA = -E_{LUMO} \quad (1)$$

$$IP = -E_{HOMO} \quad (2)$$

The chemical potential (μ), absolute electronegativity (χ) and absolute hardness (η) were calculated from a combination of ionization energy and electron affinity values using following equations [48]:

$$\chi = -\mu = \frac{IP + EA}{2} \quad (3)$$

$$\eta = \frac{IP - EA}{2} \quad (4)$$

and $$\sigma = \frac{1}{\eta} \quad (5)$$

(σ denotes the softness).

Recently, Udhayakalaa et al. have reported theoretical calculations of some quinoxaline derivatives, and one of them (namely 2,3-diphenyl quinoxaline, DPQ) has obvious structural similarity to our synthesized quinoxaline derivative [49]. Quantum chemical parameters of *N*-alkylated isomer were also computed for comparison. The obtained results of quantum chemical parameters of *O*- and *N*-alkylated isomers along with those of DPQ are reported in Table 5. A substantial E_{HOMO} value indicates a higher tendency to donate electrons, whereas, in contrast, a lower E_{LUMO} value indicates a higher ability to accept electrons [50,51]. On the other hand, the HOMO–LUMO energy gap is an excellent way for scientists to characterize the chemical reactivity and stability of molecules. Large energy gap indicates higher stability and low reactivity to a chemical species, and vice versa, if its value is lower [50,52].

Table 5. Quantum chemical parameters of DPQ *O*- and *N*-alkylated isomers obtained using DFT at the B3LYP level.

Parameter	Value		
	O-alkylated isomer	DPQ [49]	*N*-alkylated isomer
E_{HOMO}, (eV)	-6.144	-6.068	-6.204
E_{LUMO}, (eV)	-2.099	-1.906	-2.342
ΔE, (eV)	4.045	4.161	3.862
IP, (eV)	6.144	6.068	6.204
EA, (eV)	2.099	1.906	2.342
Ƞ, (eV)	2.022	2.080	1.931
χ, (eV)	4.121	3.987	4.273
ω, (eV)	4.199	3.819	4.728

σ, (eV^{-1})	0.494	0.480	0.518
ε, (eV-1)	0.238	0.261	0.211

The calculated HOMO/LUMO energies values tabulated in Table 5 are -6.144 eV / -2.099 eV, -6.068 eV / -1.906 eV, and -6.204 eV / -2.342 eV for *O*-alkylated isomer, DPQ, and *N*-alkylated isomer, respectively. Thus, the ability of *O*-alkylated isomer to donate electrons is lower than DPQ, but it is higher than that of *N*-alkylated isomer. In contrast, its ability (i.e., *O*-alkylated isomer) to accept electrons is higher than DPQ, but it is lower than that of *N*-alkylated isomer. As stated before, the energy gap between HOMO and LUMO would reveal information about the stability of a chemical compound and whether it is a soft or hard molecule. As for the energy gap values between HOMO and LUMO, these are 4.045 eV, 4.161 eV, and 3.862 for *O*-alkylated isomer, DPQ and *N*-alkylated isomer, respectively. It can be observed that *N*-alkylated isomer exhibits the lowest energy gap compared to *O*-alkylated isomer and DPQ. A molecule with a smaller energy gap is, in most cases, softer than that with a large energy gap. Thus, the DPQ and *O*-alkylated isomer compounds can be classified as hard molecules (high kinetic stability), while the *N*-alkylated isomer molecule is a soft molecule (more reactive).

The electrophilicity index (ω) and its multiplicative inverse i.e., the nucleophilicity index (ε) were calculated using the following formulas [53,54]:

$$\omega = \frac{\mu^2}{2\eta} \quad (6)$$

$$\varepsilon = \frac{1}{\omega} \quad (7)$$

Other theoretical descriptors that can be used to interpret the electron-accepting ability of molecules are the electrophilicity and the chemical potential. A strong electrophilic character is associated with a molecule that has a higher electrophilicity [55]. While, the

electron-donating ability is associated with the nucleophilicity descriptor, and this means that a molecule that has a large nucleophilicity value should have a strong nucleophilic character [55]. Therefore, results in Table 5 suggest that the synthesized *N*-alkylated isomer is the strongest electrophile, followed by *O*-alkylated isomer and DPQ compounds. In summary, quantum chemical parameters revealed that both *N*- and *O*-alkylated isomers have remarkable electronic properties. Such characteristics could make them useful for a large range of applications.

3.5. Local reactivity: Fukui functions and dual descriptor

Besides global reactivity descriptors of molecules, a more accurate study using Fukui functions could examine possibly important reactive sites and predict in a precise way the susceptibility of atoms of a molecule to a radical attack, a nucleophilic attack and an electrophilic attack [43]. The condensed Fukui functions resulted from a derivative of electron density keeping the positions of nuclei unchanged [56–58]. Nucleophilic, electrophilic, and radical attack are, respectively, expressed as (f^{+}), (f^{-}) and (f^{0}). They are defined as follows [59]:

$$f_{\mathrm{k}}^{+} = q_{\mathrm{k}}(N+1) - q_{\mathrm{k}}(N) \quad (8)$$

$$f_{\mathrm{k}}^{-} = q_{\mathrm{k}}(N) - q_{\mathrm{k}}(N-1) \quad (9)$$

$$f_{\mathrm{k}}^{0} = \frac{1}{2}\left[q_{\mathrm{k}}(N+1) - q_{\mathrm{k}}(N-1)\right] \quad (10)$$

where q_{k} is the atomic charge at the k$^{\mathrm{th}}$ atomic site within a molecule in its neutral (N), anionic (N+1) or cationic (N-1) state [60].

Further, one of the more accurate ways to predict the electrophilic and nucleophilic susceptibility is to use the dual descriptor. It has been introduced via the following equation [61]:

$$\Delta f(\mathrm{k}) = f_{\mathrm{k}}^{+} - f_{\mathrm{k}}^{-} \quad (11)$$

The dual descriptor can easily predict the propensity toward electrophilic and nucleophilic attacks. An atom susceptible to nucleophilic attack has a positive dual descriptor while that prone for electrophilic attack has a negative dual descriptor [62].

The values of condensed Fukui functions and dual descriptor are reported in Table 6. In light of the results presented in Table 6, it may be concluded that C1, C31, C32, and C22 are the most suitable sites for the radical attack. Whereas the C4, C1, C11, N14, C22, and C29, C31, C36, and C32 are the preferred atomic sites for nucleophilic and electrophilic attacks, respectively. The dual descriptor is fundamental to characterize the reactivity of atomic sites towards a nucleophilic or an electrophilic attack. However, it would be interesting to note that some sites possess both nucleophilic and electrophilic properties. For instance, C6, N13, and O40 atoms exhibit both nucleophilic and electrophilic characters. Further inspection of the results in Table 6, it can be observed that, based on the number of sites, the *O*-alkylated isomer compound has widespread electrophilic sites compared to nucleophilic ones. However, nucleophilic sites are more intense than electrophilic sites.

While FMOs provided important information about the overall reactivity of the synthesized molecule. Fukui functions calculations indicate that the reported molecule has a mix of both electrophilic and nucleophilic characteristics. Thus, highlights its donor-acceptor interactions with other chemical species.

372 **Table 6.** Condensed Fukui functions and dual descriptor of 2-(benzyloxy)-3-
373 phenylquinoxaline obtained by DFT at the GGA level.

Atom	f^0	f^+	f^-	Δf
C (6)	3.6	4.3	2.9	1.4
C (5)	2.3	3	1.7	1.3
C (4)	3.8	4.9	2.8	**2.1**
C (3)	3.5	4.3	2.8	1.5
C (2)	2.3	2.8	1.7	1.1
C (1)	**4.3**	5.6	3.1	**2.5**
N (13)	3.1	3.3	2.9	0.4
C (12)	3	3.6	2.4	1.2
C (11)	3.4	4.5	2.3	**2.2**
N (14)	3.5	4.6	2.5	**2.1**
O (40)	3.5	4.1	3	1.1
C (26)	1.3	1.2	1.3	-0.1
C (29)	2	0.3	3.7	**-3.4**
C (31)	**4.2**	1.4	7.1	**-5.7**
C (34)	2.3	1	3.6	-2.6
C (36)	3	1	5	**-4**
C (32)	**4.5**	1.5	7.5	**-6**
C (30)	2.1	0.9	3.3	-2.4
C (15)	3.7	4.5	2.9	1.6
C (16)	2.9	3.6	2.1	1.5
C (18)	2.8	3.5	2.1	1.4
C (22)	**5.2**	6.3	4.1	**2.2**
C (20)	2.7	3.2	2.1	1.1
C (17)	3.2	4	2.4	1.6

374 The actual values have been multiplied by 100 for an easier comparison. H atoms are not shown.
375

376 **3.6. Molecular electrostatic potential (MEP)**

377

378 The concept of molecular electrostatic potential is widely applied as a theoretical concept to
379 explore electrophilic, nucleophilic, and hydrogen bonding sites [63]. The prediction of the
380 reactivity of molecules by MEP can be achieved by visual inspection of different colors,
381 which represent different values of the MEP and its magnitude [64]. The most
382 electronegative electrostatic potential is represented by Red color (most substantial
383 repulsion), while blue color represents the maximum positive region (most potent attraction)

[42]. Colored areas in green mainly represent a neutral potential [42]. The increment of electrostatic potential decreases gradually from negative to positive as follows red < orange < yellow < green < blue. In the MEP maps shown in Figure 7, the maximum negative regions are mainly over N14 atom, with a significant density over the phenyl ring linked to the quinoxaline moiety and a very less density over N13 atom. In the case of positive potential, MEP showed that the maximum positive region is over hydrogen atoms. Therefore, these results confirm and strengthen the indication that the quinoxaline moiety of the *O*-alkylated isomer possesses excellent electrical properties with a wide range of electrophilic and nucleophilic sites.

3.7. Net charges

Although much of theoretical information about a molecule's reactivity can be obtained from global descriptors and Fukui functions, it is essential to mention that the charge distribution on the molecule provides an important way in the effective investigation of the charge transfer, thus donor and acceptor properties of molecule's atoms [44]. Even more important, it has the strongest influence on the overall properties of molecules such as local and global reactivity and electrophilic/nucleophilic nature. To extract charge distribution information about the quinoxaline derivative, two simple methods were utilized: the Mulliken charges and natural atomic charges. Predicting the charge distribution using the Mulliken population analysis is a widely used method because of its simplicity. However, its results can be easily varied by altering the size of the employed basis set. In contrast, the natural population analysis is known as a more reliable method. In the present work, both populations are used, and their results are graphically represented in Figure 8.

As could be seen in Figure 8(a), NPA reveals that N13, N14, and O40 (N13 = -0.493, N14 = -0.406, and O40 = -0.538) are the most negative atoms while C11, C12, and C3 (C11 = 0.173, C12 = 0.538, and C3 = 0.138) present in the adjacent positions are the most positive atoms. In the case of MPA (Figure 8(b)), N13 (-0.478), N14 (-0.479) and O40 (-0.550) are the most negative atoms whereas C12 (0.440), C3 (0.182), and C4 (0.179) are the most positive sites. The charge distribution showed that carbon atoms attached to electronegative atoms (nitrogen and oxygen) have positive charges. These electronegative atoms pull out the partial charges from the carbon atom, and hence they become positive, and it is the reason why these heteroatoms are more negative. Carbon atoms that carry higher positive charges are the most able to receive electrons from the orbital of donor species to create a feedback band. While atoms having negative charges are the most susceptible sites to give electrons to an acceptor to be bonded as a correlative. These findings are in agreement with above-mentioned MESP and Fukui functions results, which all confirm the remarkable reactivity of the quinoxaline moiety of the *O*-alkylated isomer, especially its heteroatoms.

3.8. Natural bond orbital (NBO) analysis

The NBO analysis is another crucial way to elucidate the chemical characteristics of the bonding. It can be used as a convenient means to investigate intra and intermolecular bonding, reactivity, stability, basicity, and relationship between the donor (filled orbitals) and acceptor (virtual orbitals) [65]. This analysis could permit a better understanding of charge transfer or conjugative interactions and how these interactions will affect the stability of a molecular system [43]. For more accurate information on donor-acceptor interactions, stabilization energy $E(2)$, which can be obtained from the second-order Fock-matrix

analysis, is another proficient way of gaining an insight into such information. Its value is directly proportional to the NBO interaction intensities. The strength of the molecular interaction between electron donors and electron acceptors increases with the increase of the stabilization energy, and therefore, the extent of charge transfer or conjugation of the whole system becomes more pronounced. In other words, higher NBO interaction strengths (intensities) are associated with higher stabilization energy *E*(2), thus a higher degree of electron delocalization [65].

Based on these, donor-acceptor interactions having stabilization energy above 5 kcal/mol are listed in Table S2. The highest donor-acceptor interaction is via LP (2) O40 corresponding to acceptors BD*(2) C12 - N13 with stabilization energy of 39.74 kJ/mol.

Several donor-acceptor interactions have been identified with high intensity, such as π(C15-C16) → π*(C18-C22) (20.85 kcal/mol) and π(C18-C22) → π*(C15-C16) (20.93 kcal/mol). Here, the intra-molecular interaction is formed by the orbital overlap between π (C-C) and π*(C-C) bond orbital, which results in intra-molecular charge transfer causing stabilization of the system. Donor-acceptor interactions like π(C15-C16) → π*(C18-C22) (20.85 kcal/mol), π(C18-C22) → π*(C15-C16) (20.93 kcal/mol), π(C29-C30) → π*(C32-C36) (19.89 kcal/mol) and π(C32-C36) → π*(C29-C30) (20.13 kcal/mol) are responsible for conjugation of the respective π bonds in the phenyl rings. From the quinoxaline moiety, an important interaction also leads to the stability of the title molecule. This includes the donation of lone pairs of LP(1) N13 to antibonding σ*(C11-C12) that corresponds to a stabilization energy of 11.69 kcal/mol. Together, these results demonstrate the intensive interactions between electron-donors and electron-acceptors and a greater degree of hyperconjugation in the whole system.

3.9. MD simulations: Radial distribution functions

Bearing in mind that various potential pharmaceutical compounds will eventually end-up in contact with water, information on how water molecules are positioned around the atoms of the synthesized compound could serve as a valuable tool for evaluating its stability [66]. Herein, this was examined through RDF after performing MD simulations. The RDF represents the probability of finding a particle in the distance *r* from another particle [67]. Thus, atoms with pronounced interactions with water molecules could be identified. Figure S12 summarizes the results of atoms that are more prone to interactions with water molecules. In RDF analysis, the first pronounced peak located at a short distance indicates significant interactions with water molecules [68,69]. In Figure S12, atoms C5, C4, C11, C34, C32, C20, H9, H8, H39, H38, H35, N14, N13, and O40 are represented. Results indicate that C4, C11, and C34 atoms have the significant interactions, among which, the most critical interactions could occur at C11 and C34 (peak distance at 2.29 Å and maximal g(r) value of 1.14 (C34) and 1.06 (C11)). In the case of nitrogen atoms, the first prominent peaks of N14 and N13 are located at 2.5 and 3.49 Å with a maximal g(r) values of 0.67 and 0.66, respectively. Consequently, it may be concluded that the N14 atom has the most significant interactions with water molecules. In addition to carbon and nitrogen atoms, H8 and H39 have also shown remarkable interactions with water molecules, H8 (3.10Å, 1.12) and H39 (3.3Å, 1.16). Other atoms are located at distances equal to or higher than 3.5 Å, and thus have less significant interactions with water molecules. According to these results, the investigated quinoxaline derivatives possesses significant interactions with water molecules, which indicate its instability in water. This suggests that hydrolysis and spontaneous degradation can be expected.

4. Conclusions

A novel quinoxaline derivative, 2-(benzyloxy)-3-phenylquinoxaline was synthesized, and its structure was determined by X-ray crystallography. Further, its molecular structure was examined using the Hirshfeld topology analysis and Density Functional Theory (DFT) at B3LYB employing 6-311++G(d,p) basis set. Fukui function analysis, which was obtained in the solid phase, suggested that the potentially important reactive centres of the quinoxaline derivative are C1, C31, C32 and C22 for radical attack whereas the C4, C1, C11, N14, C22, and C29, C31, C36 and C32 are the preferred sites for nucleophilic and electrophilic attacks, respectively. The FMOs distribution has shown that the quinoxaline moiety is the main responsible for donor-acceptor interactions. The MEP analysis however, indicates that the most negative region is located over the N14 atom. In order to gain an insight into the molecular stability of the synthesized compound, its intramolecular charge transfer behavior, and donor-acceptor interactions, NBO analysis was performed. The most intense donor-acceptor interaction was found to occur between LP (2) O40 and BD*(2) C12 - N13 that has a stabilization energy of 39.74 kJ/mol. RDFs obtained from MD simulations indicate that C4, C11, C34 carbon atoms, nitrogen atom N14, and hydrogen atoms H8 and H39 exhibit significant interactions with water molecules.

Conflict of interest:

The authors of this manuscript have no conflict of interest to declare.

Acknowledgements

"The authors extend their appreciation to the Deanship of Scientific Research at King Khalid University for funding this work through research groups program under grant number R.G.P. 2/94/41"

References

[1] Y. Ramli, E.M. Essassi, Advances in synthetic approaches, functionnalization and biological properties of Quinoxaline derivatives, Adv. Chem. Res. 27 (2015) 109–160.

[2] Y. Ramli, M. Missioui, M. El Fal, M. Ouhcine, E.M. Essassi, J.T. Mague, 2-{3-[2-(2-Chlorophenyl) ethyl]-2-oxo-1, 2-dihydroquinoxalin-1-yl} acetohydrazide, IUCrData. 2 (2017) x171424.

[3] R. Griffith, S. Chittur, Y. CHEN, Inhibition of Glucosamine-6-phosphate Synthase from Candida Albicans by Quinoxaline-2, 3-diones., ChemInform. 24 (1993) no-no.

[4] M. Loriga, S. Piras, P. Sanna, G. Paglietti, Quinoxaline chemistry. Part 7. 2-[aminobenzoates]-and 2-[aminobenzoylglutamate]-quinoxalines as classical antifolate agents. Synthesis and evaluation of in vitro anticancer, anti-HIV and antifungal activity., Farm. Soc. Chim. Ital. 1989. 52 (1997) 157–166.

[5] M.M. Badran, K.A. Abouzid, M.H.M. Hussein, Synthesis of certain substituted quinoxalines as antimicrobial agents (part II), Arch. Pharm. Res. 26 (2003) 107.

[6] S. Wagle, A.V. Adhikari, N.S. Kumari, Synthesis of some new 2-(3-methyl-7-substituted-2-oxoquinoxalinyl)-5-(aryl)-1, 3, 4-oxadiazoles as potential non-steroidal anti-inflammatory and analgesic agents, (2008).

[7] X. Hui, J. Desrivot, C. Bories, P.M. Loiseau, X. Franck, R. Hocquemiller, B. Figadere, Synthesis and antiprotozoal activity of some new synthetic substituted quinoxalines, Bioorg. Med. Chem. Lett. 16 (2006) 815–820.

[8] A. Carta, M. Loriga, S. Piras, G. Paglietti, P.L. Colla, B. Busonera, G. Collu, R. Loddo, Synthesis of variously substituted 3-phenoxymethyl quinoxalin-2-ones and quinoxalines capable to potentiate in vitro the antiproliferative activity of anticancer drugs in multi-drug resistant cell lines, Med. Chem. 2 (2006) 113–122.

[9] Y. Ramli, A. Moussaif, H. Zouihri, H. Bourichi, E.M. Essassi, N′-(3-Methylquinoxalin-2-yl)-N′-phenylbenzohydrazide, Acta Crystallogr. Sect. E Struct. Rep. Online. 67 (2011) o1374–o1374.

[10] M. Montana, F. Mathias, T. Terme, P. Vanelle, Antitumoral activity of quinoxaline derivatives: A systematic review, Eur. J. Med. Chem. 163 (2019) 136–147. https://doi.org/10.1016/j.ejmech.2018.11.059.

[11] T. Kaushal, G. Srivastava, A. Sharma, A. Singh Negi, An insight into medicinal chemistry of anticancer quinoxalines, Bioorg. Med. Chem. 27 (2019) 16–35. https://doi.org/10.1016/j.bmc.2018.11.021.

[12] S. Tariq, K. Somakala, Mohd. Amir, Quinoxaline: An insight into the recent pharmacological advances, Eur. J. Med. Chem. 143 (2018) 542–557. https://doi.org/10.1016/j.ejmech.2017.11.064.

[13] J.A. Pereira, A.M. Pessoa, M.N.D.S. Cordeiro, R. Fernandes, C. Prudêncio, J.P. Noronha, M. Vieira, Quinoxaline, its derivatives and applications: A State of the Art review, Eur. J. Med. Chem. 97 (2015) 664–672. https://doi.org/10.1016/j.ejmech.2014.06.058.

[14] S.V. Karakashev, M.J. Reginato, Progress toward overcoming hypoxia-induced resistance to solid tumor therapy, Cancer Manag. Res. 7 (2015) 253–264. https://doi.org/10.2147/CMAR.S58285.

[15] M. Beraud, D. Gaillard, R. Derache, Relations entre la structure chimique de quinoxalines disubstituees en positions 2,3 et les activites de detoxication enzymatique

554 des microsomes hepatiques du rat, Biochem. Pharmacol. 24 (1975) 1505–1509.
555 https://doi.org/10.1016/0006-2952(75)90027-1.
556 [16] Knowles C O, Chemistry and toxicology of quinoxaline, organotin, organofluorine, and
557 formamidine acaricides., Environ. Health Perspect. 14 (1976) 93–102.
558 https://doi.org/10.1289/ehp.761493.
559 [17] T.P. Selby, L.R. Denes, J.J. Kilama, B.K. Smith, Aryl-Substituted Quinoxalines and
560 Related Heteroarenes as Novel Herbicides Prepared via Palladium-Catalyzed Cross-
561 Coupling Methods, in: Synth. Chem. Agrochem. IV, American Chemical Society, 1995:
562 pp. 171–185. https://doi.org/10.1021/bk-1995-0584.ch016.
563 [18] K.R. Justin Thomas, J.T. Lin, Y.-T. Tao, C.-H. Chuen, Quinoxalines Incorporating
564 Triarylamines: Potential Electroluminescent Materials with Tunable Emission
565 Characteristics, Chem. Mater. 14 (2002) 2796–2802.
566 https://doi.org/10.1021/cm0201100.
567 [19] X. Xu, G. Yu, S. Chen, C. Di, Y. Liu, Synthesis and characterization of a quinoxaline
568 compound containing polyphenylphenyl and strong electron-accepting groups, and its
569 multiple applications in electroluminescent devices, J. Mater. Chem. 18 (2008) 299–
570 305. https://doi.org/10.1039/B710139B.
571 [20] T.E.A. Frizon, R.C. Duarte, J.L. Westrup, J.M. Perez, G. Menosso, L.G.T.A. Duarte,
572 J.C. Germino, M.M. Faleiros, T.D. Zambon Atvars, E. Zapp, F.S. Rodembusch, A.G.
573 Dal-Bó, Synthesis, electrochemical, thermal and photophysical characterization of
574 quinoxaline-based π-extended electroluminescent heterocycles, Dyes Pigments. 157
575 (2018) 218–229. https://doi.org/10.1016/j.dyepig.2018.04.059.
576 [21] V.A. Mamedov, N.A. Zhukova, Chapter 2 - Progress in Quinoxaline Synthesis (Part 1),
577 in: G.W. Gribble, J.A. Joule (Eds.), Prog. Heterocycl. Chem., Elsevier, 2012: pp. 55–
578 88. https://doi.org/10.1016/B978-0-08-096807-0.00002-6.
579 [22] Y. Ramli, K. Karrouchi, E. Essassi, L. El Ammari, N′-Phenyl-N′-[3-(2, 4, 5-triphenyl-2, 5-
580 dihydro-1H-pyrazol-3-yl) quinoxalin-2-yl] benzohydrazide, Acta Crystallogr. Sect. E
581 Struct. Rep. Online. 69 (2013) o1320–o1321.
582 [23] N. Abad, Y. Ramli, N.K. Sebbar, M. Kaur, E. Essassi, J. Jasinski, 1-[(1-Butyl-1H-1, 2,
583 3-triazol-5-yl) methyl]-3-methylquinoxalin-2 (1H)-one, IUCrData. 3 (2018) x180482.
584 [24] M. Missioui, M. El Fal, J. Taoufik, E. Essassi, J. Mague, Y. Ramli, 2-(3-Methyl-2-oxo-1,
585 2-dihydroquinoxalin-1-yl) acetic acid dihydrate, IUCrData. 3 (2018) x180882.
586 [25] G.M. Sheldrick, SHELXT: Integrating space group determination and structure
587 solution, Acta Crystallogr Sect Found Adv. 70 (2014) C1437.
588 [26] A. Frisch, gaussian 09W Reference, Wallingford USA 25p. (2009).
589 [27] R. Dennington, T. Keith, J. Millam, GaussView, Version 4.1. 2, Semichem Inc
590 Shawnee Mission KS. (2007).
591 [28] A.D. Becke, Density-functional exchange-energy approximation with correct
592 asymptotic behavior, Phys. Rev. A. 38 (1988) 3098.
593 [29] A.D. Becke, A new mixing of Hartree–Fock and local density-functional theories, J.
594 Chem. Phys. 98 (1993) 1372–1377.
595 [30] A.D. Becke, Becke's three parameter hybrid method using the LYP correlation
596 functional, J Chem Phys. 98 (1993) 5648–5652.
597 [31] J.P. Perdew, K. Burke, M. Ernzerhof, Generalized gradient approximation made
598 simple, Phys. Rev. Lett. 77 (1996) 3865.
599 [32] D. Studio, Accelrys Inc, San Diego CA USA. (2013).
600 [33] H. Sun, COMPASS: an ab initio force-field optimized for condensed-phase applications
601 overview with details on alkane and benzene compounds, J. Phys. Chem. B. 102
602 (1998) 7338–7364.

[34] J. Bernstein, R.E. Davis, L. Shimoni, N. Chang, Patterns in hydrogen bonding: functionality and graph set analysis in crystals, Angew. Chem. Int. Ed. Engl. 34 (1995) 1555–1573.
[35] C.F. Mackenzie, P.R. Spackman, D. Jayatilaka, M.A. Spackman, CrystalExplorer model energies and energy frameworks: extension to metal coordination compounds, organic salts, solvates and open-shell systems, IUCrJ. 4 (2017) 575–587.
[36] F.L. Hirshfeld, Bonded-atom fragments for describing molecular charge densities, Theor. Chim. Acta. 44 (1977) 129–138.
[37] M.A. Spackman, D. Jayatilaka, Hirshfeld surface analysis, CrystEngComm. 11 (2009) 19–32.
[38] M.A. Spackman, J.J. McKinnon, D. Jayatilaka, Electrostatic potentials mapped on Hirshfeld surfaces provide direct insight into intermolecular interactions in crystals, CrystEngComm. 10 (2008) 377–388.
[39] D. Jayatilaka, D. Grimwood, A. Lee, A. Lemay, A. Russel, C. Taylor, S. Wolff, P. Cassam-Chenai, A. Whitton, TONTO-A System for Computational Chemistry, (2005).
[40] J.J. McKinnon, D. Jayatilaka, M.A. Spackman, Towards quantitative analysis of intermolecular interactions with Hirshfeld surfaces, Chem. Commun. (2007) 3814–3816.
[41] K.O. Rachedi, T.-S. Ouk, R. Bahadi, A. Bouzina, S.-E. Djouad, K. Bechlem, R. Zerrouki, T. Ben Hadda, F. Almalki, M. Berredjem, Synthesis, DFT and POM analyses of cytotoxicity activity of α-amidophosphonates derivatives: Identification of potential antiviral O,O-pharmacophore site, J. Mol. Struct. 1197 (2019) 196–203. https://doi.org/10.1016/j.molstruc.2019.07.053.
[42] S. Uzun, Z. Esen, E. Koç, N.C. Usta, M. Ceylan, Experimental and density functional theory (MEP, FMO, NLO, Fukui functions) and antibacterial activity studies on 2-amino-4- (4-nitrophenyl) -5,6-dihydrobenzo [h] quinoline-3-carbonitrile, J. Mol. Struct. 1178 (2019) 450–457. https://doi.org/10.1016/j.molstruc.2018.10.001.
[43] R.I. Al-Wabli, K.S. Resmi, Y. Sheena Mary, C. Yohannan Panicker, M.I. Attia, A.A. El-Emam, C. Van Alsenoy, Vibrational spectroscopic studies, Fukui functions, HOMO-LUMO, NLO, NBO analysis and molecular docking study of (E)-1-(1,3-benzodioxol-5-yl)-4,4-dimethylpent-1-en-3-one, a potential precursor to bioactive agents, J. Mol. Struct. 1123 (2016) 375–383. https://doi.org/10.1016/j.molstruc.2016.07.044.
[44] N.A. Ancın, S.G. Öztaş, Ö. Küçükterzi, N.A. Öztaş, Theoretical investigation of N-trans-cinnamylidene-m-toluidine by DFT method and molecular docking studies, J. Mol. Struct. 1198 (2019) 126868. https://doi.org/10.1016/j.molstruc.2019.07.115.
[45] P. Bultinck, H.D. Winter, W. Langenaeker, J.P. Tollenare, Computational Medicinal Chemistry for Drug Discovery, CRC Press, 2003.
[46] S. Sakthivel, T. Alagesan, S. Muthu, C.S. Abraham, E. Geetha, Quantum mechanical, spectroscopic study (FT-IR and FT - Raman), NBO analysis, HOMO-LUMO, first order hyperpolarizability and docking studies of a non-steroidal anti-inflammatory compound, J. Mol. Struct. 1156 (2018) 645–656. https://doi.org/10.1016/j.molstruc.2017.12.024.
[47] Y. Oueslati, S. Kansız, A. Valkonen, T. Sahbani, N. Dege, W. Smirani, Synthesis, crystal structure, DFT calculations, Hirshfeld surface, vibrational and optical properties of a novel hybrid non-centrosymmetric material (C10H15N2) 2H2P2O7, J. Mol. Struct. 1196 (2019) 499–507.
[48] N. Islam, S. Kaya, Conceptual Density Functional Theory and Its Application in the Chemical Domain, CRC Press, 2018.

[49] P. Udhayakalaa, T. Rajendiranb, S. Gunasekaranc, Quantum chemical investigations on some quinoxaline derivatives as effective corrosion inhibitors for mild steel, Pharm. Lett. 4 (2012) 1285–1298.
[50] M.E. Mashuga, L.O. Olasunkanmi, E.E. Ebenso, Experimental and theoretical investigation of the inhibitory effect of new pyridazine derivatives for the corrosion of mild steel in 1 M HCl, J. Mol. Struct. 1136 (2017) 127–139. https://doi.org/10.1016/j.molstruc.2017.02.002.
[51] Ş. Erdoğan, Z.S. Safi, S. Kaya, D.Ö. Işın, L. Guo, C. Kaya, A computational study on corrosion inhibition performances of novel quinoline derivatives against the corrosion of iron, J. Mol. Struct. 1134 (2017) 751–761. https://doi.org/10.1016/j.molstruc.2017.01.037.
[52] H. Shokry, Molecular dynamics simulation and quantum chemical calculations for the adsorption of some Azo-azomethine derivatives on mild steel, J. Mol. Struct. 1060 (2014) 80–87. https://doi.org/10.1016/j.molstruc.2013.12.030.
[53] P.K. Chattaraj, U. Sarkar, D.R. Roy, Electrophilicity index, Chem. Rev. 106 (2006) 2065–2091.
[54] R.G. Parr, L. v Szentpaly, S. Liu, Electrophilicity index, J. Am. Chem. Soc. 121 (1999) 1922–1924.
[55] L.H. Madkour, S. Kaya, L. Guo, C. Kaya, Quantum chemical calculations, molecular dynamic (MD) simulations and experimental studies of using some azo dyes as corrosion inhibitors for iron. Part 2: Bis–azo dye derivatives, J. Mol. Struct. 1163 (2018) 397–417. https://doi.org/10.1016/j.molstruc.2018.03.013.
[56] W. Guerrab, I.-M. Chung, S. Kansiz, J.T. Mague, N. Dege, J. Taoufik, R. Salghi, I.H. Ali, M.I. Khan, H. Lgaz, Synthesis, structural and molecular characterization of 2, 2-diphenyl-2H, 3H, 5H, 6H, 7H-imidazo [2, 1-b][1, 3] thiazin-3-one, J. Mol. Struct. 1197 (2019) 369–376.
[57] A. Dutta, S.Kr. Saha, P. Banerjee, D. Sukul, Correlating electronic structure with corrosion inhibition potentiality of some bis-benzimidazole derivatives for mild steel in hydrochloric acid: Combined experimental and theoretical studies, Corros. Sci. 98 (2015) 541–550. https://doi.org/10.1016/j.corsci.2015.05.065.
[58] H. Lgaz, I.-M. Chung, R. Salghi, I.H. Ali, A. Chaouiki, Y. El Aoufir, M.I. Khan, On the understanding of the adsorption of Fenugreek gum on mild steel in an acidic medium: Insights from experimental and computational studies, Appl. Surf. Sci. 463 (2019) 647–658. https://doi.org/10.1016/j.apsusc.2018.09.001.
[59] H. Mi, G. Xiao, X. Chen, Theoretical evaluation of corrosion inhibition performance of three antipyrine compounds, Comput. Theor. Chem. 1072 (2015) 7–14. https://doi.org/10.1016/j.comptc.2015.08.023.
[60] S.Kr. Saha, P. Ghosh, A. Hens, N.C. Murmu, P. Banerjee, Density functional theory and molecular dynamics simulation study on corrosion inhibition performance of mild steel by mercapto-quinoline Schiff base corrosion inhibitor, Phys. E Low-Dimens. Syst. Nanostructures. 66 (2015) 332–341. https://doi.org/10.1016/j.physe.2014.10.035.
[61] C. Morell, A. Grand, A. Toro-Labbe, New dual descriptor for chemical reactivity, J. Phys. Chem. A. 109 (2005) 205–212.
[62] W. Guerrab, I.-M. Chung, S. Kansiz, J.T. Mague, N. Dege, J. Taoufik, R. Salghi, I.H. Ali, M.I. Khan, H. Lgaz, Synthesis, structural and molecular characterization of 2, 2-diphenyl-2H, 3H, 5H, 6H, 7H-imidazo [2, 1-b][1, 3] thiazin-3-one, J. Mol. Struct. 1197 (2019) 369–376.
[63] M. Raja, R. Raj Muhamed, S. Muthu, M. Suresh, Synthesis, spectroscopic (FT-IR, FT-Raman, NMR, UV–Visible), NLO, NBO, HOMO-LUMO, Fukui function and molecular

docking study of (E)-1-(5-bromo-2-hydroxybenzylidene)semicarbazide, J. Mol. Struct. 1141 (2017) 284–298. https://doi.org/10.1016/j.molstruc.2017.03.117.

[64] S.H. Rosline Sebastian Sr., M.I. Attia, M.S. Almutairi, A.A. El-Emam, C.Y. Panicker, C. Van Alsenoy, FT-IR, FT-Raman, molecular structure, first order hyperpolarizability, HOMO and LUMO analysis, MEP and NBO analysis of 3-(adamantan-1-yl)-4-(prop-2-en-1-yl)-1H-1,2,4-triazole-5(4H)-thione, a potential bioactive agent, Spectrochim. Acta. A. Mol. Biomol. Spectrosc. 132 (2014) 295–304. https://doi.org/10.1016/j.saa.2014.04.177.

[65] Z. Demircioğlu, Ç.A. Kaştaş, O. Büyükgüngör, Theoretical analysis (NBO, NPA, Mulliken Population Method) and molecular orbital studies (hardness, chemical potential, electrophilicity and Fukui function analysis) of (E)-2-((4-hydroxy-2-methylphenylimino)methyl)-3-methoxyphenol, J. Mol. Struct. 1091 (2015) 183–195. https://doi.org/10.1016/j.molstruc.2015.02.076.

[66] J.A. War, K. Jalaja, Y.S. Mary, C.Y. Panicker, S. Armaković, S.J. Armaković, S.K. Srivastava, C. Van Alsenoy, Spectroscopic characterization of 1-[3-(1H-imidazol-1-yl)propyl]-3-phenylthiourea and assessment of reactive and optoelectronic properties employing DFT calculations and molecular dynamics simulations, J. Mol. Struct. 1129 (2017) 72–85. https://doi.org/10.1016/j.molstruc.2016.09.063.

[67] R.V. Vaz, J.R.B. Gomes, C.M. Silva, Molecular dynamics simulation of diffusion coefficients and structural properties of ketones in supercritical CO2 at infinite dilution, J. Supercrit. Fluids. 107 (2016) 630–638. https://doi.org/10.1016/j.supflu.2015.07.025.

[68] B. Sureshkumar, Y.S. Mary, K.S. Resmi, C.Y. Panicker, S. Armaković, S.J. Armaković, C. Van Alsenoy, B. Narayana, S. Suma, Spectroscopic analysis of 8-hydroxyquinoline derivatives and investigation of its reactive properties by DFT and molecular dynamics simulations, J. Mol. Struct. 1156 (2018) 336–347. https://doi.org/10.1016/j.molstruc.2017.11.120.

[69] S. Arshad, R. Raveendran Pillai, D.A. Zainuri, N.C. Khalib, I.A. Razak, S. Armaković, S.J. Armaković, R. Renjith, C.Y. Panicker, C. Van Alsenoy, Synthesis, XRD crystal structure, spectroscopic characterization, local reactive properties using DFT and molecular dynamics simulations and molecular docking study of (E)-1-(4-bromophenyl)-3-(4-(trifluoromethoxy)phenyl)prop-2-en-1-one, J. Mol. Struct. 1137 (2017) 419–430. https://doi.org/10.1016/j.molstruc.2017.02.045.

Figures captions:

Figure 1. (a) The title molecule with labeling scheme and 50% probability ellipsoids, (b) the optimized molecular structure of the title compound by DFT at B3LYB.

Figure 2. Packing viewed along the b-axis direction with intermolecular interactions shown as in Fig. S1.

Figure 3. The full two-dimensional fingerprint plots for the title compound, showing (a) all interactions, and delineated into (b) H···H, (c) C···H/H···C and (d) N···H/H···N interactions. The d_i and d_e values are the closest internal and external distances (in Å) from given points on the Hirshfeld surface contacts.

Figure 4. Hirshfeld surface representations with the function d_{norm} plotted onto the surface for (a) All···All, (b) H···H, (c) C···H/H···C and (d) N···H/H···N interactions.

Figure 5. Percentage contributions of interatomic contacts to the Hirshfeld surface for the title compound.

Figure 6. Frontier molecular orbitals (HOMO and LUMO) of 2-(benzyloxy)-3-phenylquinoxaline.

Figure 7. The molecular electrostatic potential map of 2-(benzyloxy)-3-phenylquinoxaline.

Figure 8. Atomic charges of 2-(benzyloxy)-3-phenylquinoxaline obtained by (a) NBO and (b) Mulliken analyses.

Figure 1.

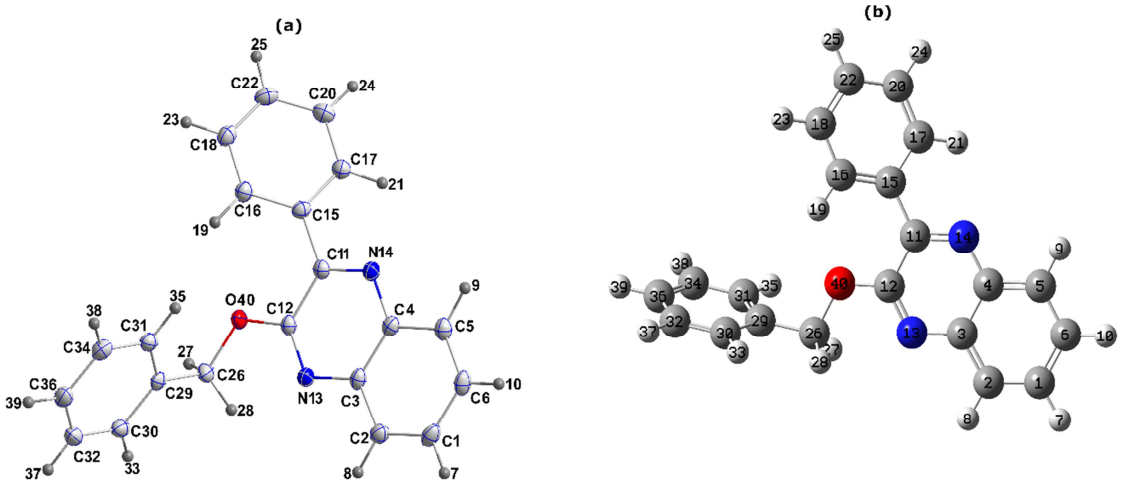

Figure 2.

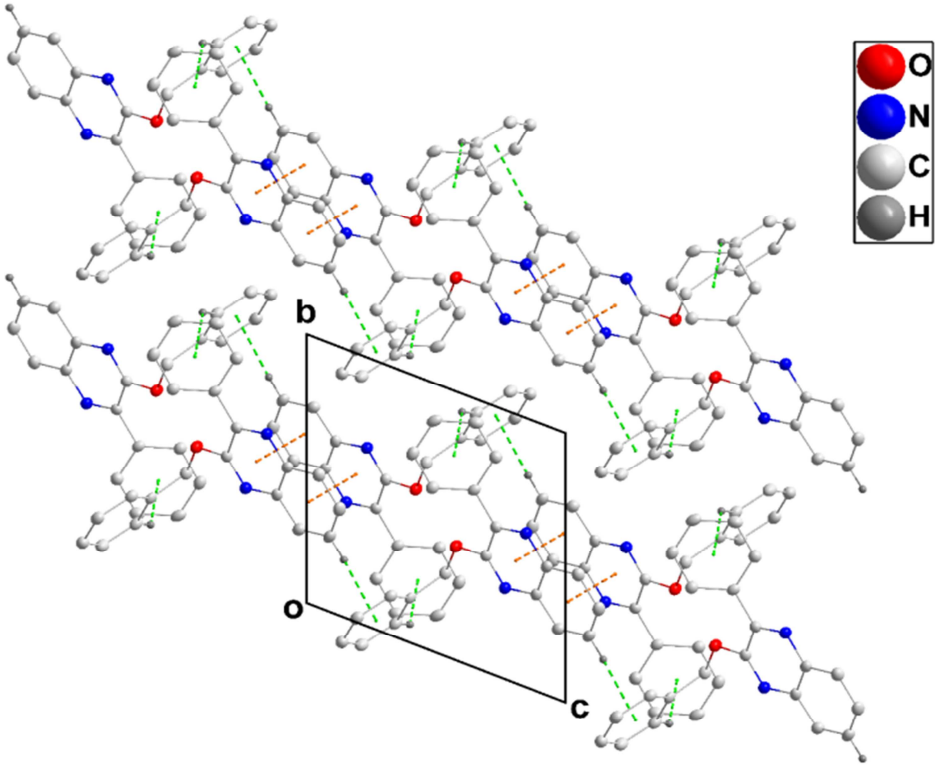

Figure 3.

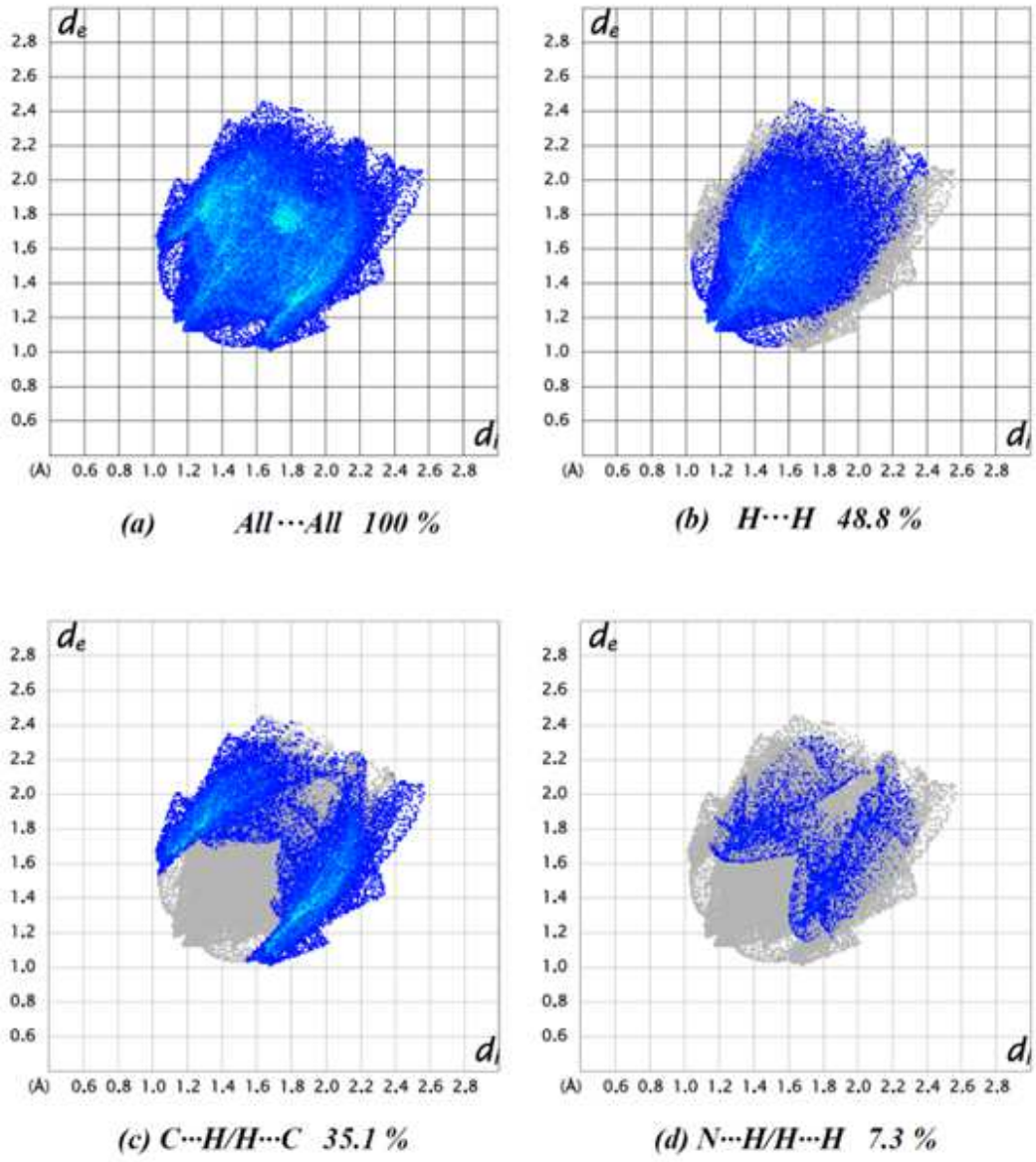
d_e
d_i
(Å) 0.6 0.8 1.0 1.2 1.4 1.6 1.8 2.0 2.2 2.4 2.6 2.8
(a) All···All 100 %
(b) H···H 48.8 %
(c) C···H/H···C 35.1 %
(d) N···H/H···H 7.3 %

Figure 4.

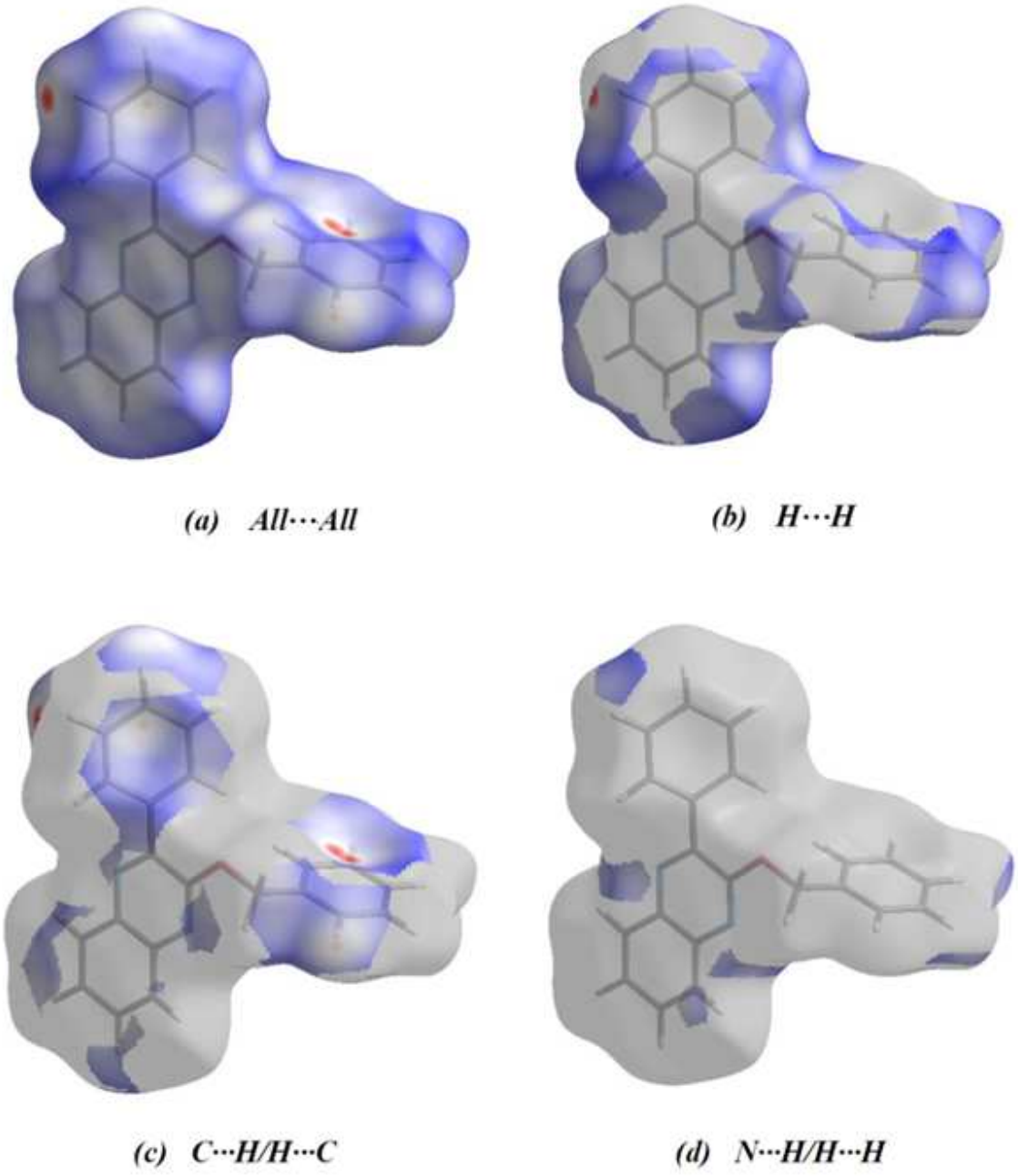

(a) All···All

(b) H···H

(c) C···H/H···C

(d) N···H/H···H

Figure 5.

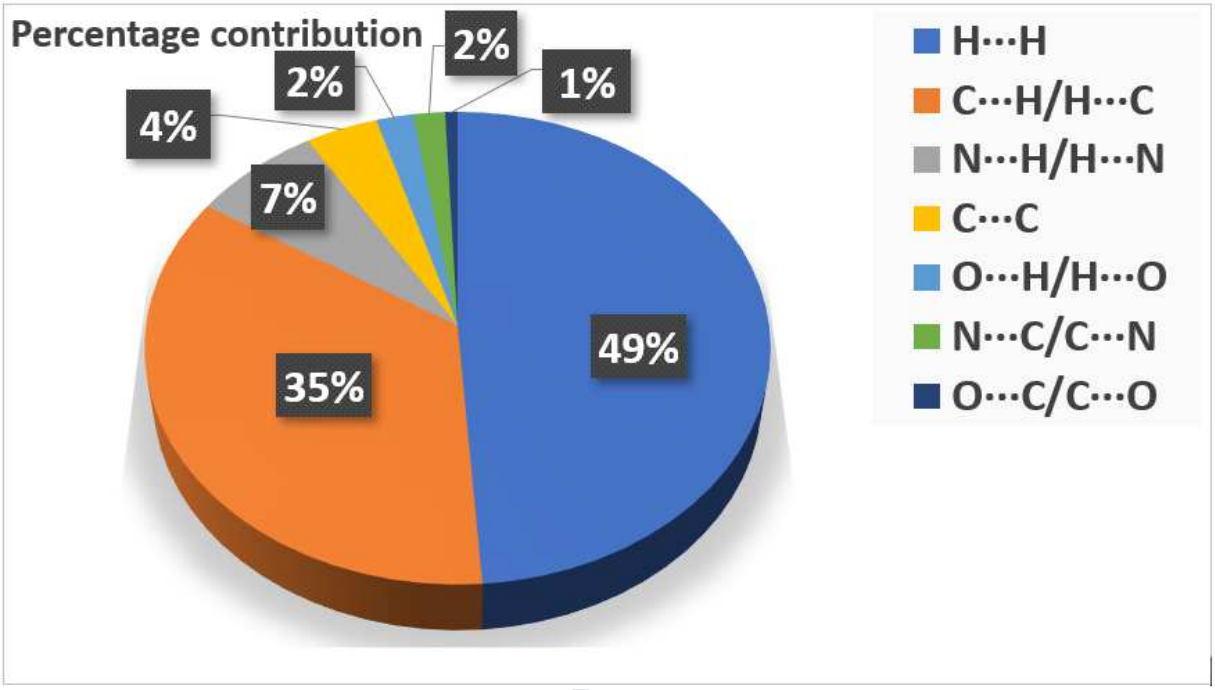

Figure 6.

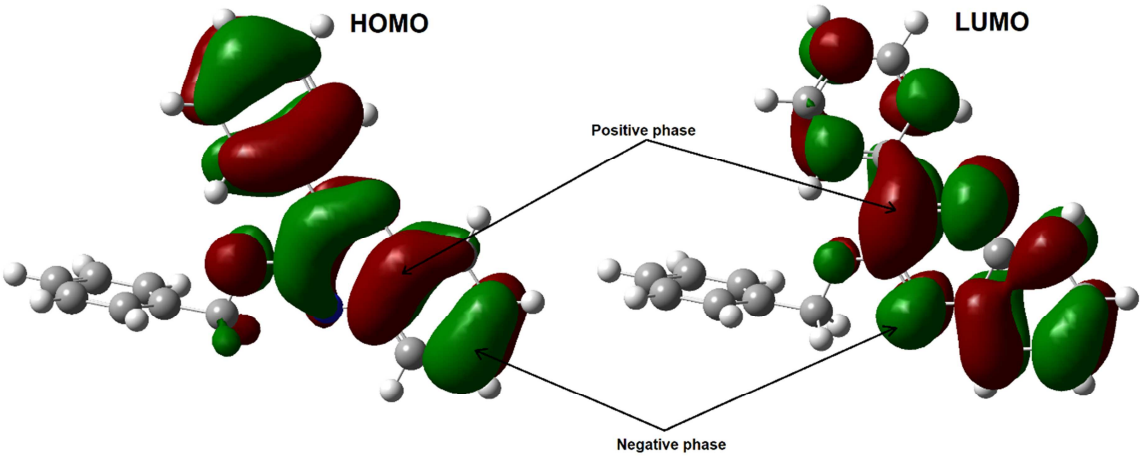

Figure 7.

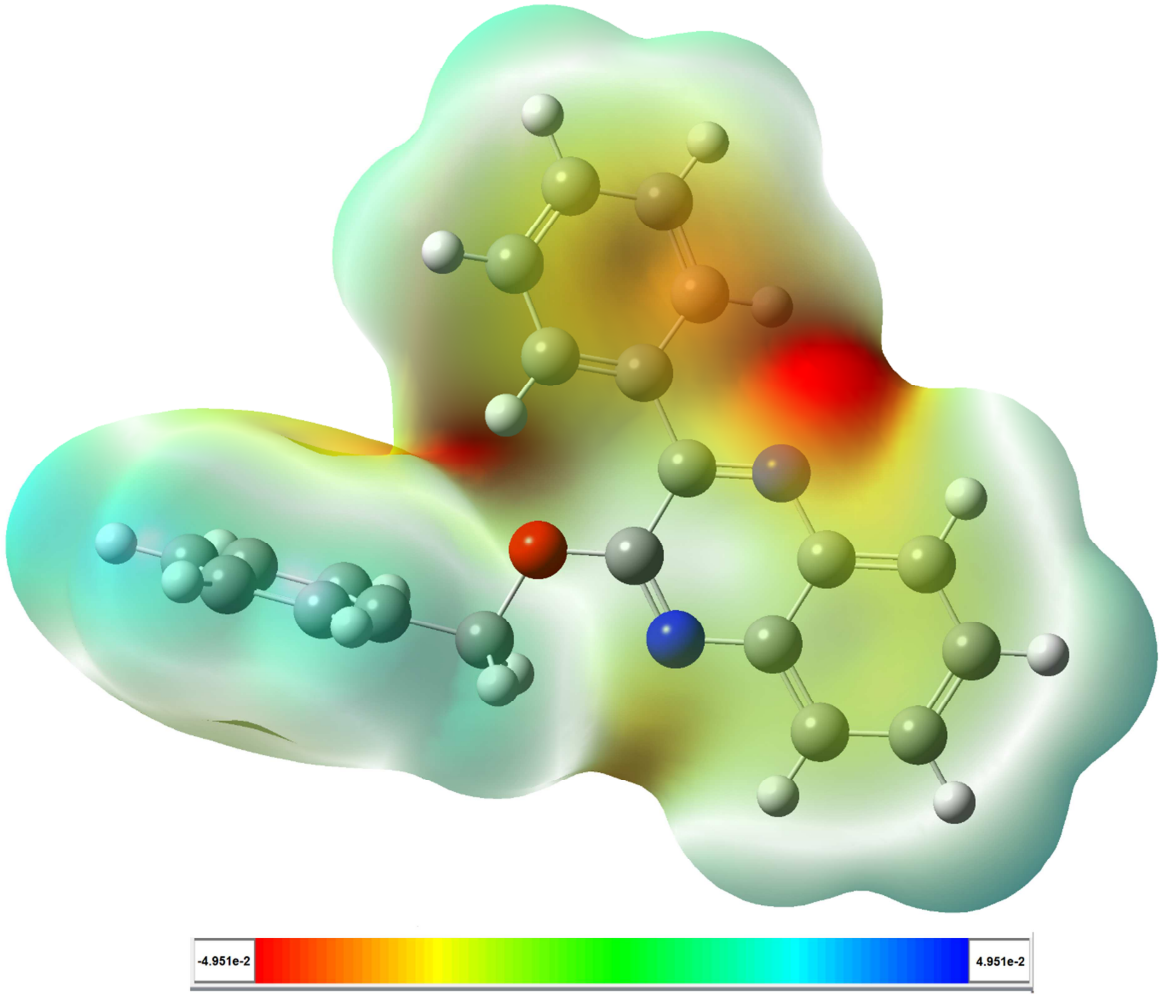

Figure 8.

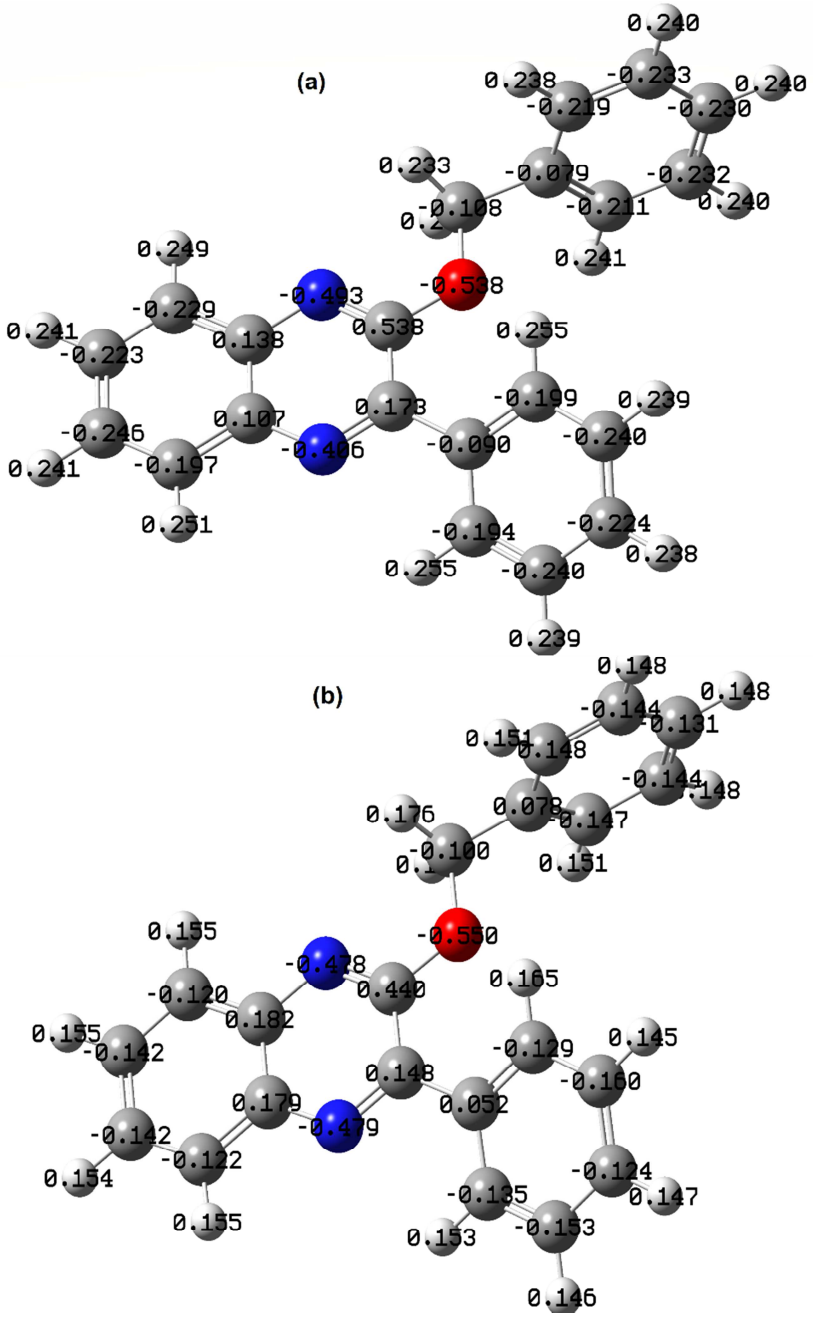
(a)
0.240
0.238
-0.233
0.240
-0.219
-0.230
0.233
-0.079
-0.232
-0.108
-0.211
0.240
0.241
0.249
-0.538
-0.493
-0.229
0.241
0.538
0.255
0.138
-0.223
-0.199
0.239
0.173
0.107
-0.245
-0.240
-0.090
-0.406
0.241
-0.197
0.251
-0.194
-0.224
0.238
0.255
-0.240
0.239
(b)
0.148
0.148
-0.144
0.131
0.151
0.148
-0.144
0.148
0.176
0.078
0.147
-0.100
0.151
0.155
-0.550
-0.438
0.440
0.165
-0.120
0.182
0.155
-0.142
-0.129
0.145
0.148
-0.160
0.179
0.052
-0.142
-0.479
-0.122
0.154
-0.124
0.147
-0.135
0.155
0.153
-0.153
0.146

- 2-(benzyloxy)-3-phenylquinoxaline has been synthesized and characterized by XRD.
- DFT, NBO, Fukui function analysis and radial distribution function have been carried out.
- The XRD parameters were compared with the theoretical data.
- Hirshfeld surface analysis of crystal structure was studied.

Conflict of interest:

The authors of this manuscript have no conflict of interest to declare.